Journal of Catalysis 287 (2012) 114–123

Contents lists available at SciVerse ScienceDirect

Journal of Catalysis

journal homepage: www.elsevier.com/locate/jcat

# Mechanistic study of preferential CO oxidation on a Pt/NaY zeolite catalyst

Jing Xu, Xin-Chao Xu, Like Ouyang, Xue-Jing Yang, Wei Mao, Junjie Su, Yi-Fan Han *

*State Key Laboratory of Chemical Engineering, East China University of Science and Technology, Shanghai 200237, People's Republic of China*

ARTICLE INFO

*Article history:*
Received 18 November 2011
Revised 12 December 2011
Accepted 13 December 2011
Available online 10 January 2012

*Keywords:*
Preferential CO oxidation
PROX
Kinetics
In situ DRIFTS
Pt clusters
Pt/zeolite
XPS
TEM

ABSTRACT

Mechanistic study of the preferential CO oxidation was carried out over a Pt(1.0 wt.%)/NaY zeolite catalyst from 300 to 523 K by combination of kinetics and spectroscopy. The mechanism of CO oxidation at 300 K was proposed on the basis of spectroscopic study, and the activity at low temperatures was assumed to originate from small Pt clusters. The analysis of XPS and TEM revealed that metallic state of Pt was rather stable after the reaction. The kinetics suggests a Langmuir–Hinshelwood mechanism in the oxygen-limited low-rate branch ($O_2$ adsorption/dissociation is strongly depressed by adsorbed CO), being responsible for CO oxidation in $H_2$-rich gas in the temperature range of 423–523 K. In situ DRIFT spectra show that the Pt surface is dominated by linearly bound CO species, and the presence of $H_2$ leads to a significant red-shift of the C—O stretch frequency, which indicates a $H_{ad}$-induced modification of the Pt—CO bond, not just a coverage-dependent frequency shift. Consequently, CO oxidation was significantly enhanced in $H_2$-rich gas.



## 1. Introduction

The preferential oxidation of CO (PROX) for purifying $H_2$ gas from steam reforming methanol or other compounds has received increasing attention for the last years [1–6]. It is a crucial reaction for the production of pure $H_2$ supplying to the proton-exchange membrane (PEM) fuel cell, because the concentration of CO in the hydrogen feed must be kept below 100 ppm for the proper operation of PEMFC [1]. Up to now, supported noble metal catalysts, such Ru, Rh, Pt, Au, and their alloys with a second metal, have been widely studied for PROX of CO [7–13]. Among all catalysts, Pt-based catalysts have found excellent performance for this reaction because of its high durability and selectivity. It has been revealed that this reaction over Pt catalysts follows the Langmuir–Hinshelwood mechanism in the oxygen-limited low-rate branch [14–16]. However, the relationship of the structure–activity–selectivity over supported Pt catalysts is still rare.

Generally, two reactions, $2CO + O_2 \rightarrow CO_2$ and $H_2 + O_2 \rightarrow H_2O$, compete in this reaction system. Till now, most of efforts have been devoted to CO oxidation, but less attention to the effect of $H_2$ adsorption/oxidation, which also plays an essential role in evaluating the fuel efficiency and the designation of the PROX reactor. As defined in Eq. (1), the lower selectivity ($S$) toward $CO_2$ means the decrease in the amount of $H_2$ supplied into fuel cells, being equivalent to the loss of fuel efficiency. For instance, a selectivity of 50% in the PROX of CO, equal reaction rates of CO and $H_2$ oxidation, corresponds to a loss of approximately 2.7% in fuel efficiency for typical 2% vol CO in the methanol reformate.

$$S = \frac{\Delta O_2^{(CO)}}{\Delta O_2^{(CO)} + \Delta O_2^{(H_2)}} \times 100\% \quad (1)$$

A variety of Pt catalysts have been explored for this reaction by loading Pt clusters or nanoparticles on different oxide surfaces, such as $CeO_2$, $TiO_2$, MgO, $Al_2O_3$, and $SiO_2$ [13–15,17,18]. Interestingly, Pt encaged in porous materials has proven extremely high selectivity for CO oxidation. It was reported that the selectivity could be as high as 90% over a Pt/mordenite catalyst and nearly 100% over a PtFe/mordenite or porous silica catalyst (FSM) [19–24], in contrast to 45% measured for a Pt/$\gamma$-$Al_2O_3$ catalyst [14]. More recently, Fukuoka et al. [4,25] found that the promotional effects, in the case of Pt/FSM catalysts, were related with the pore size of mesoporous supports.

NaY zeolite is a type of microporous material, which is abundant of microchannels and cages that allow Pt particles to be highly distributed and stabilized. Mechanistic study of the PROX reaction over Pt/zeolite catalysts, especially CO oxidation on Pt particles less than 5.0 nm, is scarce. Several questions about the mechanism are still not clear, for instance, how does $H_2$ affect on adsorption/desorption of CO and CO oxidation in this catalytic system? Therefore, such a work, as an excellent case study, is of paramount importance for both catalyst design and practical application. Pt nanoparticles encaged in zeolite, a Pt (1.0 wt.%)/NaY catalyst, is a good model catalyst for this purpose.

* Corresponding author. Fax: +86 21 64251928.
*E-mail address:* yifanhan@ecust.edu.cn (Y.-F. Han).

0021-9517/$ - see front matter © 2011 Elsevier Inc. All rights reserved.
doi:10.1016/j.jcat.2011.12.012

In the following, we will first present kinetic data describing the dependence of the reaction rate (i) on CO partial pressure $p_{CO}$ (0.01–1.5 kPa) at constant oxygen excess $\lambda = 2$ ($\lambda$ describes the ratio $p_{O_2} : p_{CO}$, with $\lambda = 1$ for stoichiometric conditions, that is, $\lambda = (2p_{O_2} = p_{CO})$) as well as at constant oxygen partial pressure, (ii) on the $O_2$ partial pressure (at constant $p_{CO}$, that is, at varying $\lambda$), and (iii) on the reaction temperature (423–523 K). The advantages of this method have been introduced in the previous studies [14–16]. Then, spectroscopic study of the interaction of CO and the surface Pt atoms will be performed under reaction conditions. The distribution of Pt particles larger than 1.0 nm located internal pores of NaY is determined by transmission electron microscopy (TEM); the extremely small Pt particles as encaged clusters, perhaps, less than 1.0 nm, are characterized by technique of in situ diffuse reflectance infrared Fourier transform spectroscopy (DRIFTS) at different temperatures using CO as probe molecule. The chemical states of Pt over the fresh and spent catalyst are determined by X-rays photon spectroscopy (XPS) in combination with in situ DRIFTS. Finally, in combination with the spectroscopic results and kinetics of CO oxidation, a plausible mechanism will be proposed to elucidate the behavior of PROX of CO on zeolite supported Pt catalysts.

## 2. Experimental

### 2.1. Catalyst Preparation

Iron-free faujasite NaY (Si/Al = 2.76) was prepared by hydrothermal crystallization [26]. The exchange of Pt (1.0 wt.%) into the zeolite and the autoreduction of the specimens followed the approaches reported previously [27]. Briefly, Pt was introduced as the tetra-ammine ion complex from $10^{-3}$ M aqueous solutions of the chloride. The loaded zeolites were washed until chloride-free and dried at 373 K. Both the NaY zeolite and the solution were analyzed by an inductively coupled plasma optical emission spectrometer (ICP, Perkin Elmer). The autoreduction of the specimens was carried out using a temperature program with a ramping rate of 1 K/min in a Ar flow (20 mL/min).

### 2.2. Kinetic measurements

Kinetic measurements were carried out using a microfix-bed reactor; a quartz tube with an ID of 4 mm was located in a ceramic tube oven and under differential conditions with typically 50–100 mg catalyst powder (catalyst bed length 5–8 mm). Before reaction, the catalyst was conditioned by calcination in a 10% $O_2/N_2$ stream (20 mL/min) at 673 K for 30 min and then reduced at 573 K in $H_2$ (20 mL/min) for another 30 min. The conversion of CO was kept below 5.0% at $p_{CO} > 0.1$ kPa, and below 10.0% at $p_{CO} < 0.1$ kPa by diluting the catalyst with $\alpha$-$Al_2O_3$, which is inert for $CO/H_2$ oxidation under current conditions. Reactions were carried out at a temperature range 423–523 K in two different atmospheres: a $H_2$-free gas (0.1–1.5 kPa CO and 0.3–2.0 kPa $O_2$, rest $N_2$) and a $H_2$-rich gas (0.01–1.5 kPa CO and $O_2$, $\lambda = 2$, 75 kPa $H_2$, rest $N_2$). Influent and effluent gases were analyzed with an online gas chromatograph (Shimadzu GC-2010) equipped with a CP-carbonBOND column. Each data point was taken at an interval of 2 h. High-purity reaction gases (CO 4.7, $O_2$ 5.0, $H_2$ 5.0, $N_2$ 6.0) were used. Evaluation of the Weisz criterion showed the absence of mass transport–related problems [28]. The catalyst is rather stable, CO conversion was gradually decreased by about 15% after running for 1000 min at 523 K (1.0 kPa $CO/O_2$, $\lambda = 2$, 75 kPa $H_2$, rest $N_2$). The effects of products ($H_2O$ and $CO_2$), the maximum concentration of $H_2O$ (0.075%), and $CO_2$ (0.15%) imposed no effect on the reaction rate.

Absolute reaction rate of CO ($r_{CO}$) and $H_2$ ($r_{H_2}$) oxidation in the simulated reformate is expressed as Eqs. (2) and (3), respectively. In the ideal reformate, $r_{H_2}$ is calculated for the average concentration of oxygen, $\dot{c}_{O_2}$, at the inlet and outlet of the reactor (Eq. (4)):

$$r_{CO} = \frac{\dot{c}_{CO,in} \cdot X_{CO} \cdot \dot{V}_{gas}}{m_{Me}} \quad [\text{mol s}^{-1}\ \text{g}_{Me}^{-1}] \tag{2}$$

$$r_{H_2} = r_{CO}\left(\frac{1}{S} - 1\right) \tag{3}$$

$$r_{O_2} = \frac{\dot{c}_{O_2,in} \cdot X_{O_2} \cdot \dot{V}_{gas}}{m_{Me}} \quad [\text{mol s}^{-1}\ \text{g}_{Me}^{-1}] \tag{4}$$

$m_{Me}$ is the mass of Pt in the reactor bed, $\dot{V}_{gas}$ is total molar flow rate, $X_{CO}$ is CO conversion based on $CO_2$ formation in the simulated reformate, $X_{O_2}$ is $O_2$ conversion, $S$ is selectivity for CO oxidation, and $\dot{c}_{CO}, \dot{c}_{O_2}$ is the concentration of CO, $O_2$ in gas mixture, equal to $p_i/p_0$, $p_i$: partial pressure of reactants, $p_0$: total pressure in the system.

Consequently, the selectivity in $H_2$-rich gas can then be calculated as:

$$S = \frac{0.5 \times c_{CO_2}^{out}}{c_{O_2}^{in} - c_{O_2}^{out}} = \frac{0.5 \times c_{CO_2}^{out}}{\Delta c_{O_2}} \tag{5}$$

### 2.3. DRIFTS

All DRIFTS of CO adsorption were performed in an in situ reaction cell (modified Harricks model HV-DR2) in order to allow gas flowing continuously through the catalyst bed (ca. 0.1 g) during spectra acquisition. The spectra were recorded on a PerkinElmer FT-IR spectrum 100 (resolution: 4 $cm^{-1}$) spectrometer connected a GC-QMS (HPR-20, Hiden Analytical Ltd.), equipped with an MCT narrow-band detector, by co-adding 300 single-beam spectra, equivalent to an acquisition time of ~5 min. All infrared data were evaluated in Kubelka–Munk units, which were linearly related to the absorber concentration in DRIFTS. Spectral contributions from gaseous CO were eliminated by subtracting the corresponding spectra from the pure support material. For CO adsorption at room temperature, typically, 100 single-beam spectra at a nominal resolution of 8 $cm^{-1}$ were added for one spectrum, equivalent to an acquisition time of ~30 s. Prior to every measurement, all samples were in situ conditioned using the same procedure as given in the kinetic measurements.

### 2.4. XPS

X-ray photoelectron spectra were collected with a VG ESCALAB 250 spectrometer, using Al K$\alpha$ radiation (1486.6 eV, pass energy 20.0 eV) at a base pressure of $1 \times 10^{-9}$ Torr. The background contribution (obtained by the Shirley method) arising from inelastic processes was subtracted, while curve-fitting employed a Gaussian–Lorentzian profile. The binding energies (BEs) were calibrated internally against Si 2p (103.5 eV) and C 1s (285.0 eV) peaks and externally with a Au wire (Au 4f at 84.0 eV). The reduced catalysts were protected by ultra high-purity $N_2$ when cooling down to room temperature. To eliminate systematic errors, the reference materials were cleaned by Ar ion etching for 5 min at 3.0 μA. The uncertainty of XPS results caused by air will be minimized by comparing the reference spectra of fresh reduced sample. Note that due to the overlap of the Pt 4f and Al 2p level in the range of 70–75 eV, the separation of Al 2p peak in the Pt 4f region was referred to the Al 2p = 73.9 eV in the Pt-free NaY zeolite; the deconvolution of the Pt 4f level was referred to a core level energy of metallic $Pt^0$ 4f 7/2 at 70.1 eV.

### 2.5. TEM

Microstructure and morphology of the catalyst were determined by TEM, which was performed on a 200-keV microscope (Philips CU-20-ST). The catalyst was suspended in ethanol, and one drop of this slurry was deposited on a carbon-coated copper grid. The liquid phase was evaporated before the grid was loaded into the microscope.

## 3. Results

### 3.1. Kinetic measurements

#### 3.1.1. Partial pressure dependence – reaction orders

Before the kinetic measurements, it was verified that contributions from side reactions, such as CO and $CO_2$ methanation or the forward and reverse gas-shift reaction, were negligible for the current reaction parameters. $CO_x$ methanation was measured only at 573 K, yielding less than 0.1% $CH_4$; while the rates for the water gas-shift reaction were lower than those of CO oxidation by 2–3 magnitudes.

*3.1.1.1. $H_2$-rich gas.* The dependence of the CO oxidation rate on $p_{CO}$ was investigated in the partial pressure range 0.01–1.5 kPa at 423, 473, and 523 K, respectively, at a constant $O_2$ excess of $\lambda = 2$ (Fig. 1a and b). The reaction rates decay continuously with decreasing $p_{CO}$. The logarithmic reaction rates are proportional to the logarithmic $p_{CO}$ over the entire pressure range investigated (Fig. 1a). Assuming a simple power law description of the reaction rate, $r_{CO}$, with

$$\ln(r_{CO}) = \ln(k_{CO}) - \frac{Ea}{R \cdot T} + \boldsymbol{\alpha}_{CO} \cdot \ln(p_{CO}) + \boldsymbol{\alpha}_{O_2} \cdot \ln(p_{O_2}), \quad (6)$$

this indicates a constant reaction order. For constant $\lambda$, as in the present case, the slope of the resulting lines yields the overall reaction order $\alpha'_{CO}$, which in this description is related to the reaction orders for CO and $O_2$, $\alpha_{CO}$, and $\alpha_{O_2}$, respectively, by $\alpha'_{CO} = \alpha_{CO} + \alpha_{O_2}$. The $\alpha'_{CO}$ derived from those experiments are 0.28, 0.51, and 0.56 for 423, 473, and 523 K, respectively (Table 1). At $p_{CO} = 1.0$ kPa, $r_{CO}$ increased by a factor of 100 from 423 to 523 K.

A similar increase in $r_{CO}$ was observed with an increase in $p_{O_2}$ (Fig. 1c). With keeping $p_{CO} = 1.0$ kPa, and the reaction orders, $\alpha_{O_2} = 0.74$, 0.64, and 0.56 for 423, 473, and 523 K, respectively, were obtained from those slopes, whereas corresponding $\alpha_{CO}$ at −0.46, −0.13, and ~0 were derived as well (Table 1). These kinetic characteristics, negative reaction orders with respect to CO and positive to $O_2$, are consistent with the Langmuir–Hinshelwood reaction mechanism in the low-rate branch. At 523 K, however, CO oxidation is no longer an oxygen-limited, but a transition from an oxygen-limited low-rate branch to a CO-limited high-rate branch.

The selectivities for CO oxidation exhibited as a function of $p_{CO}$ and $p_{O_2}$ (Fig. 1b and d), respectively. At 423 K, the selectivity of ca. 50% was almost independent of $p_{CO}$. At 473 K, it increased from 20% at 0.01 kPa to 60% at 1.5 kPa, and the pressure dependence of the selectivity was even more pronounced at 523 K, ranging from 10% at 0.01 kPa to 60% at 1.5 kPa CO. About 30–50% increase in selectivity was also observed with an increase in $p_{O_2}$ (Fig. 1d); especially, a selectivity of ca. 80% was obtained at $p_{O_2} = 2.5$ kPa ($\lambda = 5$). Interestingly, the change in selectivity with varying $p_{O_2}$ is dependent of CO oxidation rates; $H_2$ oxidation rates (open symbols in Fig. 1c) are almost constant.

*3.1.1.2. $H_2$-free gas.* A rather similar behavior of CO oxidation was also observed in $H_2$-free gas (Fig. 2). The absolute values of $\alpha_{CO}$ and $\alpha_{O_2}$ are slightly higher than those for $H_2$-rich gas, with $\alpha_{CO} = -0.65/\alpha_{O_2} = 1.07$ at 423 K and $\alpha_{CO} = -0.78/\alpha_{O_2} = 1.22$ at 523 K. Meanwhile, under current conditions, the CO oxidation reaction rates in $H_2$-free gas are generally lower than that in $H_2$-rich gas by a factor of 2–4. Clearly, CO oxidation was remarkably improved in the presence of $H_2$.

#### 3.1.2. Temperature dependence – activation energies

Temperature-dependent rates at $p_{CO} = 0.01$, 0.2, and 1.0 kPa were plotted in an Arrhenius diagram (Fig. 3). For reaction in $H_2$-rich gas, these data can approximately be described by two linear regions, with slopes resulting in an $E_a = 54.0 \pm 4.0$ kJ/mol below 473 K and an $E_a = 90.0 \pm 5.0$ kJ/mol above 473 K. In contrast, for reaction in $H_2$-free gas, at $p_{CO} = 1.0$ kPa, a linear relationship

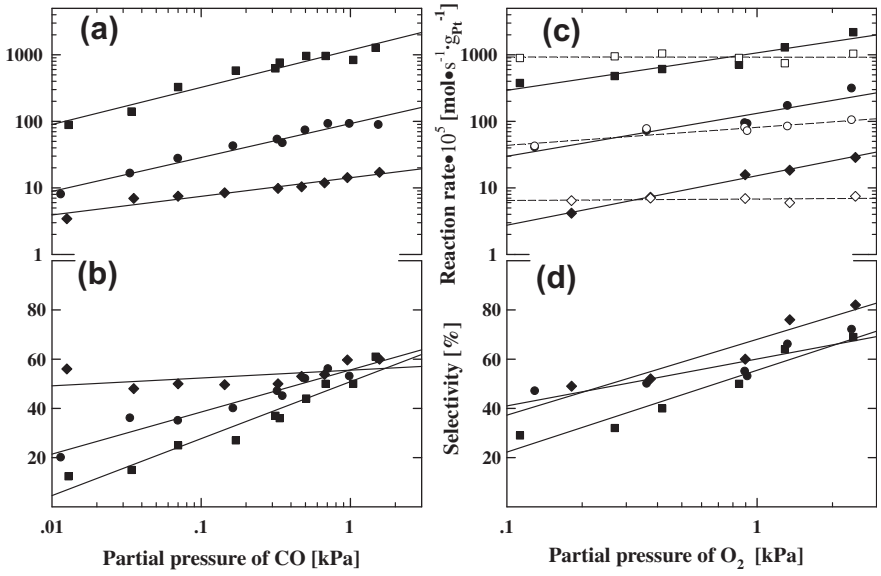


**Fig. 1.** Dependence of the CO oxidation rate $r_{CO}$ (a) and selectivity $S$ (b) on the CO partial pressure in idealized reformate gas (CO: 0.01–1.5 kPa, $\lambda = 2$, $H_2$: 75 kPa, balance $N_2$). Catalyst dilution: 1:400/20/5 with $\alpha$-$Al_2O_3$ for 423 (♦), 473 (●), and 523 K (■), respectively. Flow rate: 120/60 mL/min. Dependence of the CO oxidation rate $r_{CO}$ (c) and the selectivity $S$ (d) on the $O_2$ partial pressure in idealized reformate gas (CO: 1 kPa, $\lambda = 0.4$–5, $H_2$: 75 kPa, balance $N_2$). Catalyst dilution: 1:5–1:400 with $\alpha$-$Al_2O_3$. Flow rate: 60 mL/min in the range of 423–523 K. The dashed line and hollow symbols in (c) represent the corresponding $H_2$ oxidation rate at the respective reaction parameters.

**Table 1**
Apparent activation energies, reaction orders with respect to $p_{CO}$, $\alpha_{CO}$, and $p_{O_2}$, $\alpha_{O_2}$, for CO oxidation on supported Pt catalysts at atmospheric pressure.

| System | Reaction conditions | $T$-range (K) | $E_a$ (kJ/mol) | $\alpha_{O_2}$ | $\alpha_{CO}$ | Ref. |
|---|---|---|---|---|---|---|
| Pt/γ-$Al_2O_3$ | 0.05–1 kPa CO, $\lambda$ = 2, 75 kPa $H_2$, rest $N_2$ | 423–523 | 72–76 | +0.8 | −0.4 | [14] |
| Pt/γ-$Al_2O_3$ | 1.0 kPa CO, $\lambda$ = 1 | <473 | 55 | +1 | −1.5 | [29] |
| Pt/γ-$Al_2O_3$ | 1.0 kPa CO, $\lambda$ = 1, 2.5 kPa $H_2O$ | <473 | 45 | +1 | −0.7 | [29] |
| Pt/γ-$Al_2O_3$ | 3.0 kPa CO, $\lambda$ = 1 | 373–493 | 67–71 | +0.7 | −0.1 | [30] |
| Pt/$SiO_2$ | 1.3 kPa CO, $\lambda$ = 1 | <423–473 | 56–80 | +0.9 | −0.2 | [31] |
| Pt/$SiO_2$ | 2.0 kPa CO, $\lambda$ = 0.8 | 353 | 72–78 | +1 | <0 | [31] |
| Pt/NaY Zeolite | 0.1–1.5 kPa CO, $\lambda$ = 2, rest $N_2$ | 423–473 | 80.5–84.5 | +1.07 to 0.65 (423 K)<br>+1.22 to 0.78 (523 K) | | This work |
| Pt/NaY Zeolite | 0.01–1.5 kPa CO, $\lambda$ = 2, 75 kPa $H_2$, rest $N_2$ | 423–473<br>473–523 | 50–58<br>85–95 | +0.74 to 0.46 (423 K)<br>+0.64 to 0.13 (473 K)<br>+0.56 to 0 (523 K) | | This work |

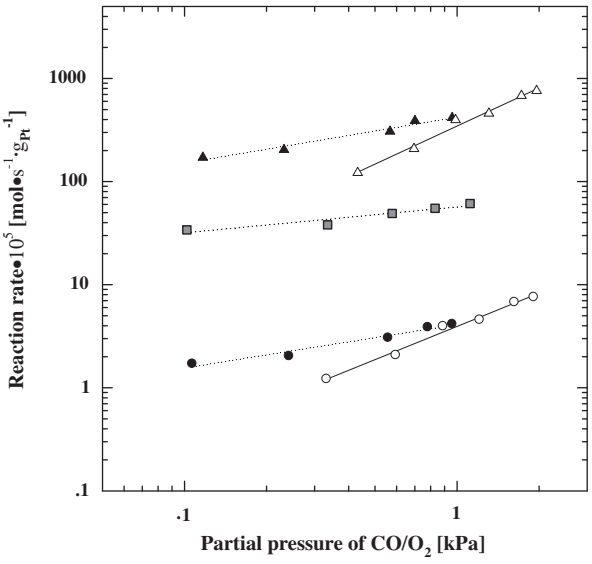


**Fig. 2.** Dependence of the CO oxidation rate $r_{CO}$ on the CO partial pressure in a $H_2$-free gas mixture (CO: 0.1–1.5 kPa, $\lambda$ = 2, balance $N_2$, dashed lines) at 423 K (●), 473 K (■), and 523 K (▲) and on the $O_2$ partial pressure in the $H_2$-free gas mixture (CO: 1 kPa, $O_2$: 0.3–2.0 kPa, rest $N_2$, solid lines) at 423 K (○) and 523 K (Δ). Catalyst dilution: 1:400/200 with α-$Al_2O_3$ for 523 and 423 K, respectively. Flow rate: 120/60 mL/min.

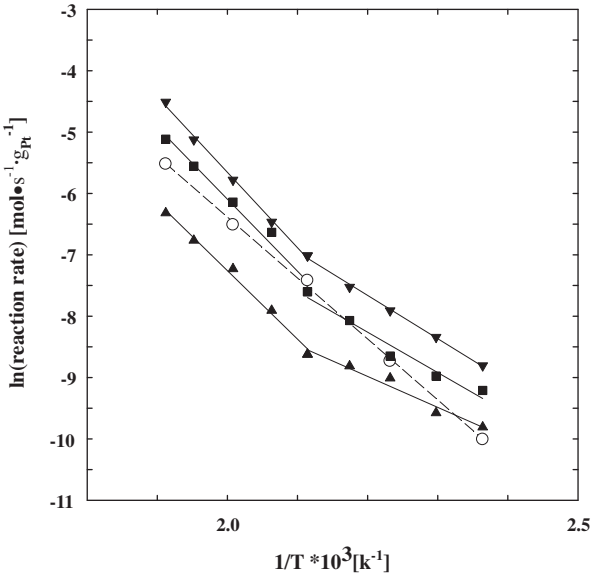


**Fig. 3.** Arrhenius diagram of ln($r_{CO}$) vs. 1/$T$ for CO oxidation in $H_2$-rich and $H_2$-free gas mixtures in the temperature range of 423–523 K. $H_2$-rich atmosphere: $p_{CO}$ = 0.01 (▼), 0.2 (■) and 1.0 kPa (▲), $\lambda$ = 2, 75 kPa $H_2$, rest $N_2$; $H_2$-free atmosphere: $p_{CO}$ = 1.0 kPa (○), rest $N_2$. Catalyst dilution: 1:5–1:400 with α-$Al_2O_3$, flow rate: 60–120 mL/min.

between the logarithmic oxidation rates and 1/$T$ was obtained for the entire temperature range, yielding an $E_a$ = 82.5 ± 2.0 kJ/mol.

### 3.2. Characterization

#### 3.2.1. TEM

Pt nanoparticles with a diameter range 2–4 nm are predominant for the fresh (Fig. 4A) and spent (Fig. 4B) catalyst, the size of most Pt particles was smaller than 4.0 nm (Fig. 4B), and the mean size (average diameter, $\bar{d}_{Pt}$) after conditioning is about 3.4 ± 0.2 nm, corresponding to a dispersion of 33.7%. The particle size was almost unchanged after reaction. In addition, extremely small Pt particles encaged in zeolite cannot be resolved by TEM, the actual particle size is expected to be smaller than 1.0 nm.

#### 3.2.2. XPS analysis

The XPS Pt 4f spectra (Fig. 5) obtained for different samples (unreacted and reacted) were recorded. On the basis of the ratio of Pt $4f_{7/2}$/Pt $4f_{5/2}$ = 4/3 [32,33] and 3.3 eV of the spin–orbit coupling between two peaks [34], the Pt $4f_{7/2}$ spectra could be deconvoluted into two peaks at 70.1 and 71.0 eV, corresponding to metallic $Pt^0$ and oxide $Pt^{2+}$, respectively. The ratio of $Pt^0/Pt^{2+}$ peak area (Table 2) revealed that metallic $Pt^0$ was predominant on the surface of the fresh catalyst; a trace amount of Pt atoms might be oxidized in the reaction as identified with the reacted catalyst. In addition, oxidative Pt has also been evidenced previously to exist inherently over the Pt/NaY zeolite catalyst even after reduction [35]. These isolated $Pt^{2+}/Pt^{4+}$ was assumed to locate in sodalite cages and hexagonal prisms of the zeolite (Supporting information, Table S1).

#### 3.2.3. In situ DRIFT spectra of CO adsorption/oxidation

*3.2.3.1. CO adsorption/oxidation at 300 K.* Time-dependant spectroscopy of CO adsorption was first recorded at 300 K in CO (1.5%)/$N_2$. With referring the previous studies for different Pt-based catalysts (Table 3), the bands ($\nu_{CO}$) in the region of 2000–2200 $cm^{-1}$ are assigned to CO linearly bound to $Pt^0$ or $Pt^{\delta+}$; the ones in the region of 1700–2000 $cm^{-1}$ are attributed to the bridge CO band. Four linear bands at 2160, 2067, 2034, and 2006 $cm^{-1}$ were clearly detected (Fig. 6). The $\nu_{CO}$ at 2067 $cm^{-1}$ can be attributed to CO bound to Pt particles larger than 1.2 nm, while the $\nu_{CO}$ at 2034 and 2006 $cm^{-1}$ may result from CO bound to Pt clusters less than 1.2 nm [44]. A weak band at 2160 $cm^{-1}$, assigned to $Pt^{2+}$—CO, suggests the existence of $Pt^{2+}$ even after pretreatment. In addition, a broad bridge band centered at 1825 $cm^{-1}$ was also clearly observed, but its intensity is almost independence of the time.

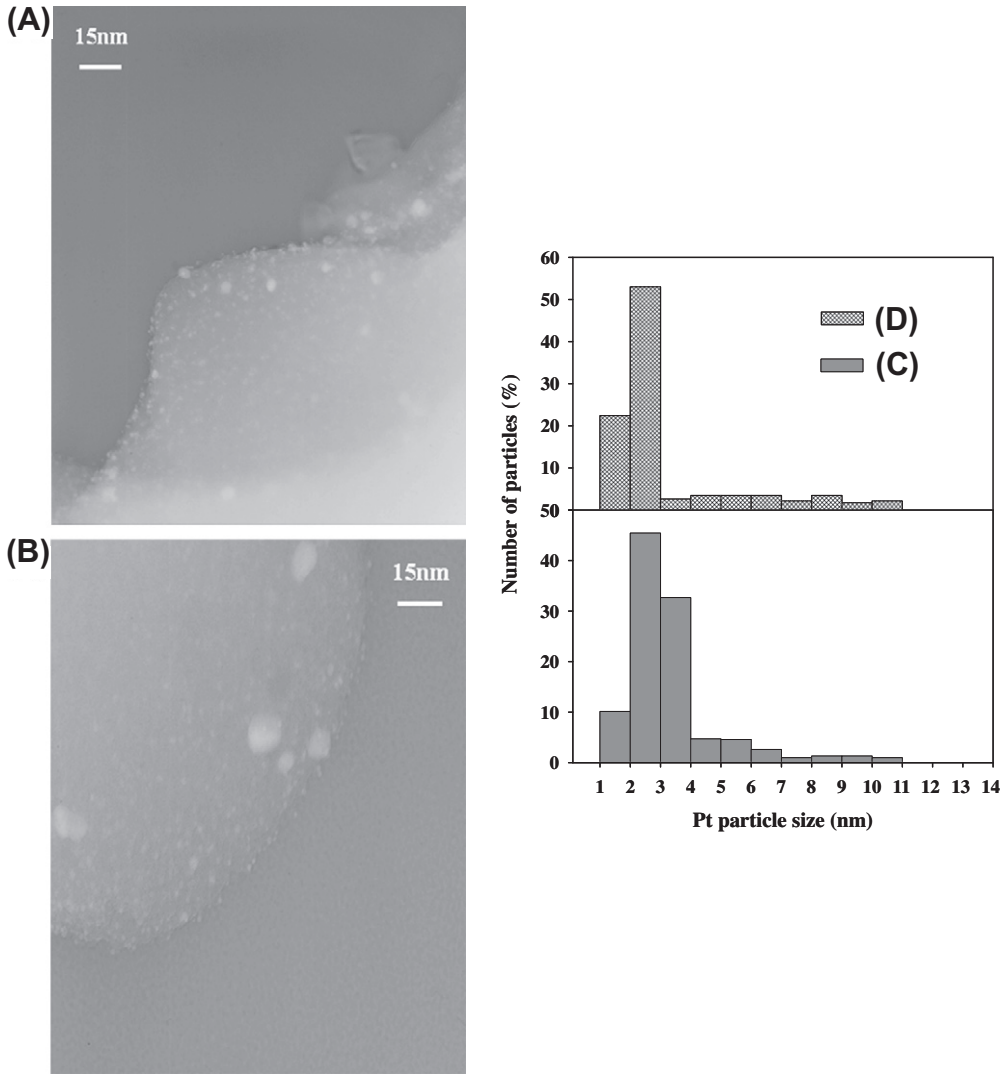


**Fig. 4.** TEM images for (A) fresh reduced (as conditioned) and (B) reacted (running for 1000 min in a mixture of 1 kPa CO, $\lambda = 2$, 75 kPa $H_2$, rest $N_2$ at 523 K) catalyst; Size distribution of (C) fresh reduced and (D) reacted Pt particles.

The time-dependent spectra (Fig. 7) for CO oxidation (CO═$O_2$ (1.5%)/$N_2$) at 300 K exhibited a maximum at 2060 $cm^{-1}$ at 30 s, eventually shifted up to 2080 $cm^{-1}$ at 750 s, while its intensity increased concurrently. The blue-shift of this band can be attributed to the co-adsorption of $CO_{ad}$ and $O_{ad}$ on the surface Pt, by which the electron (e) density of Pt particles is reduced by transferring electron to $O_{ad}$. In the same time, the intensity of the weak linear band at 2170 $cm^{-1}$, assigned to CO—$Pt^{2+}$ species, increased steadily. The bridge band at 1827 $cm^{-1}$ was observed, but its intensity was largely reduced comparing with the correspondent spectra in $O_2$-free gas (Fig. 6). Of interesting, a new peak appeared at 2357 $cm^{-1}$ during reaction. Mantell et al. [45] suggested that the band at 2353 $cm^{-1}$ should be attributed to a $CO_2$ molecule standing nearly vertical and slightly bent on Pt surface as the product from CO oxidation. The formation of this single band will be further discussed. It is noted that a similar $CO_{2ad}$ peak was observed in $H_2$-rich gas under the same reaction conditions.

*3.2.3.2. CO adsorption/oxidation in the temperature range 423–523 K.* For CO adsorption at 423 K (Fig. 8a), the spectra were slightly changed comparing to that from 300 K. Several characteristic $\nu_{CO}$ bands at 2201, 2093, 2077, and 2001 $cm^{-1}$ were observed in a stream of CO (1.5%)/$N_2$. The $\nu_{CO}$ at 2201 $cm^{-1}$ can be assigned to CO adsorbed on $Pt^{2+}$ [42–44]. A shoulder at 2093 $cm^{-1}$ is likely to result from CO bound to Pt clusters connecting to the oxygen on the wall of zeolite cages ((O)$Pt_n$—CO). The $\nu_{CO}$ at 2077 $cm^{-1}$ is attributed to CO adsorbed on Pt particles outside zeolite cages [44,46–54]. Finally, the small shoulder at 2001 $cm^{-1}$ is tentatively attributed CO bonded to small Pt clusters inside the cages [44,46–47]. Decreasing $p_{CO}$ from 1.5 to 0.04 kPa, a red-shift of $\Delta\nu = -16$ $cm^{-1}$ for the main peak at 2077 $cm^{-1}$, which is owing to the fade of adsorbate–adsorbate interactions and dynamic dipole–dipole coupling effects.

For CO adsorption in $H_2$-rich gas (Fig. 8b), the general characteristics of CO bands are rather similar to those in $H_2$-free gas, with the following modifications: (i) The $\nu_{CO}$ at 2201 $cm^{-1}$ ($Pt^{2+}$—CO) disappeared completely, (ii) the $\nu_{CO}$ at 2077 $cm^{-1}$ ($H_2$-free) was shifted down to 2054 $cm^{-1}$ ($H_2$-rich), and iii) the bridge CO was shifted from 1813 $cm^{-1}$ ($H_2$-free) to 1789 $cm^{-1}$ ($H_2$-rich). The red-shift of the main peak because of the change in $p_{CO}$ became significantly weaker upon addition of $H_2$, with $-\Delta 16$ $cm^{-1}$ in $H_2$-free gas and $-\Delta 5$ $cm^{-1}$ in $H_2$-rich gas. Hence, the shift of the C—O stretch frequency results not only from a $H_{ad}$-induced lowering of the $CO_{ad}$ coverage, but also from a modification of the Pt—CO bond due to the interaction with co-adsorbed $H_{ad}$ species. For CO adsorption at 523 K (Fig. 9a and b), the spectra were rather similar

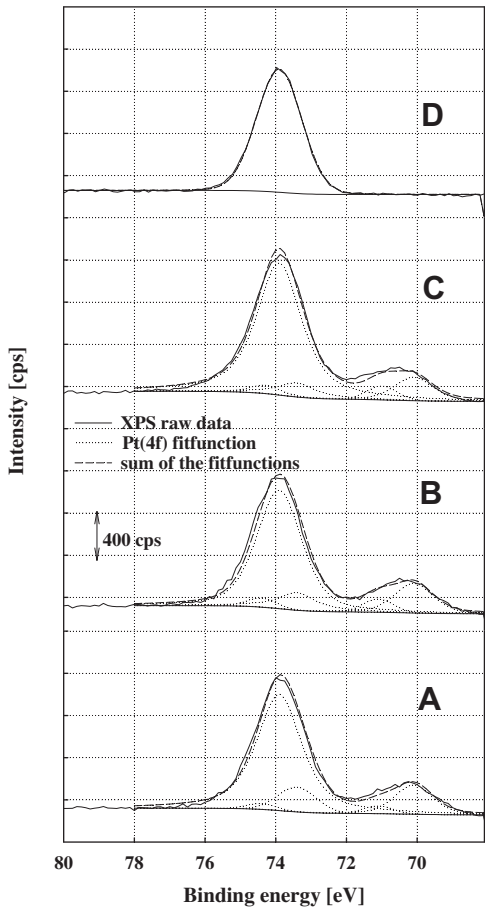


**Fig. 5.** $Pt_{4f}$ XPS spectra for (A) fresh reduced (as conditioned) and (B) reacted (running for 1000 min in a mixture of 1 kPa CO, $\lambda = 2$, 75 kPa $H_2$, rest $N_2$ at 523 K, flow rate: 120 N ml/min) catalyst; (C) oxidized catalyst (in $O_2$ (10%)/$N_2$ mixture at 673 K, 1 h) and (D) NaY zeolite.

to that obtained upon adsorption at 423 K. The only difference is that the band at 1985 $cm^{-1}$ appeared in $H_2$-rich gas (Fig. 9b).

Furthermore, $CO_{ad}$ coverage, $\theta_{CO}$, from the integrated intensities of the linear CO band in Figs. 8 and 9 was evaluated. All coverages were normalized to the saturation one ($\theta_{CO} = 1.0$) at 423 K in $H_2$-free gas with $p_{CO} = 1.5$ kPa, which is about 0.7 monolayers (ML) [15]. In $H_2$-free gas, decreasing $p_{CO}$ from 1.5 to 0.04 kPa, the correspondent $\theta_{CO}$ decreased to 0.75 at 423 K and 0.6 at 523 K (Fig. 10); the trends in $H_2$-rich gas were similar, but the $CO_{ad}$ coverages were significantly reduced, with $\theta_{CO} = 0.58$ at 423 K and $\theta_{CO} = 0.73$ at 523 K for $p_{CO} = 1.5$ kPa, which decay to $\theta_{CO} = 0.44$ and $\theta_{CO} = 0.38$ for $p_{CO} = 0.04$ kPa. This fact demonstrated that the $\theta_{CO}$ was affected by the factors such as temperature, $H_2$, and concentration of CO.

The vibrational frequencies for the linear CO bands were found to shift up with the increasing of $p_{CO}$ (Fig. 10), and it is generally attributed to a strengthening of the dipole–dipole coupling effect and static adsorbate–adsorbate interactions with an increase in $\theta_{CO}$. We argue that hydrogen adsorption not only leads to a change of $CO_{ad}$ coverage, but also a weakening of the Pt—CO interaction.

## 4. Discussion

CO oxidation over Pt clusters or model Pt catalysts has been studied for decades because it is an excellent model reaction for both fundamental study and practical application [54–57]. The evolution of the reactivities with the cluster size is correlated with the position of the atomic d-states with respect to the $O_2$ antibonding $\pi_g^*$ state; however, the implement of the same reaction in the presence of $H_2$, especially, at low temperatures, over Pt clusters loaded on zeolite has rarely been reported so far.

TEM images (Fig. 4) showed that the average size of Pt was about 3.4 nm and quite stable during reaction. It is well known that zeolite frameworks have a great deal of exchangeable cations, some exchanged Pt atoms could form extremely small clusters (<1.0 nm), which were located in the channels and cages of zeolite [58]. It was reported that a small Pt cluster consisting of null atoms (an edge length of about 0.55 nm) existed in the cage by bonding to the wall of zeolite LTL [51]. The Pt particles smaller than 1.0 nm are unlikely to be visualized by TEM because of its resolution limits. In principle, faujasites (zeolites X and Y) have a three-dimensional pore structure incorporating nearly spherical cages with a diameter of 1.2 nm. Naturally, the diameter for the Pt clusters at the cage of Y zeolite is estimated of no more than 1.2 nm. Up to now, the determination of Pt clusters less than 1.0 nm loaded on zeolites is still a challenge, even though a variety of techniques, such as EXAFS, IR, HRTEM, and chemisorption [50,58–60], have been utilized. In particular, the DRIFTS of CO adsorption may provide valuable information for this aim.

The DRIFT spectra at 300 K (Fig. 6) showed the double low-frequency $\nu_{CO}$ bands at 2034 and 2006 $cm^{-1}$. The former can be assigned to CO bound to Pt clusters with lower coordination number (<5), which leads to more back donation of Pt electrons to CO 2 $\pi^*$ orbital and the creation of low-frequency linear CO bands [44,50]. In particular, the band at 2006 $cm^{-1}$ indicates that the coordination number of Pt clusters is close to 3 or less [50], a single Pt atom or a cluster compositing of less than 5 of Pt atoms [60]. More recently, CO-IRAS spectra of Pt nanoparticles of varied size from 4.0 to 2.5 nm on $SiO_2$ demonstrated a red-shift by almost $\Delta 20$ $cm^{-1}$, while the percentage of terrace sites decreased by 50% [61].

Subsequently, a unique band at 2357 $cm^{-1}$ (Fig. 7) was observed in the mixture of CO and $O_2$ ($p_{CO} = p_{O_2} = 1.5$ kPa), while the low-frequency bands at 2034 and 2006 $cm^{-1}$ (Fig. 6)

**Table 2**
Pt4f XPS spectra: peak positions, areas, and widths.

| Sample[a] | Pt $4f_{7/2}$ | | | Pt $4f_{5/2}$ | | | $Pt^0$(70.1 eV)/$Pt^{2+}$ (71.0 eV) |
|---|---|---|---|---|---|---|---|
| | BE (eV) | Area | FWHM (eV)[c] | BE (eV) | Area | FWHM (eV) | (area ratio) |
| Reduced | 70.1 | 424 | 1.27 | 73.4 | 318 | 1.27 | 5.5 |
| | 71.0 | 77 | 1.0 | 74.3 | 58 | 1.0 | |
| CO adsorbed[a] | 70.1 | 520 | 1.27 | 73.4 | 390 | 1.27 | 4.8 |
| | 71.0 | 107 | 1.0 | 74.3 | 80 | 1.0 | |
| CO + $O_2$ adsorbed[b] | 70.1 | 518 | 1.27 | 73.4 | 384 | 1.27 | 4.8 |
| | 71.0 | 108 | 1.0 | 74.3 | 81 | 1.0 | |

[a] Adsorption of CO (1.5%) in $N_2$ over fresh reduced catalyst for 1 h at room temperature.
[b] In the stream of CO (1.5%) + $O_2$ (1.5%), rest $N_2$ over fresh reduced catalyst for 1 h at 300 K.
[c] Full-width at half maximum (FWHM) in eV.

**Table 3**
Proposed assignments of the $CO_{ad}$ bands on supported and single-crystal Pt catalysts.

| Species | Frequencies ($cm^{-1}$) | Support/Pt Single crystal | Comments | Ref. |
|---|---|---|---|---|
| $Pt^0$—CO | 2070–2076 | Pt(1 1 1) (1 1 0) | UHV | [36] |
| $Pt^0$—CO | 2095 | Pt(1 1 1) | UHV | [37] |
| $Pt^0$—CO | 2081 (face), 2070 (corner), 2063 (edge) | $SiO_2$ ($d_{Pt}$: 1.1–10.5 nm) | System pressure: $1 \times 10^{-7}$ Torr | [38] |
| $Pt^0$—CO | 2100 | $Al_2O_3$ | 300–460 K | [39] |
| $(Pt^0)_2CO$ | 1840 | $Al_2O_3$ | 300–460 K | [39] |
| $Pt^0$—CO | 2083 | $Al_2O_3$ | Pt crystal faces 423–523 K | [40] |
| $Pt^0$—CO | 2060 | $Al_2O_3$ | Pt unextend crystal faces | [40] |
| O—Pt—CO | 2120 | $Al_2O_3$ | $O_2$ + CO, 298 K | [41] |
| $Pt^{2+}$—CO | 2110 | NaY zeolite | $p_{CO}$: 72–76 kPa 353 K | [42] |
| $Pt_3(CO)_3(\mu_2\text{-}CO)_3$ | 1896, 1841 | NaY zeolite | 353 K | [42] |
| $Pt_9$ or $Pt_{12}$—CO | 2026 | NaY zeolite | 353 K | [42] |
| $Pt^0$—CO | 2078 | HZSM-5 zeolite | 300 K | [43] |
| $Pt^0$—CO | 2025–2090 (HF) 2000–2025 (LF) | NaX Zeolite | HF: $d_{Pt} > 1.2$ nm LF: $d_{Pt} < 1.2$ nm 298 K | [44] |
| $Pt^{\delta-}$—CO | 1970 | NaX Zeolite | 298 K | [46] |
| $Pt(O_{zeolite})_2(CO)_2$ | 2035, 2100 | NaX Zeolite | 298 K | [46] |
| $Pt^{\delta+}$—CO | 2100–2120 | NaY Zeolite | 298 K | [47] |
| $[Pt_3(CO)_6]_n^{2-}, n = 3, 4$ | 2040 (linear) 1840 (bridge) | Colloidal Pt | 298 K | [48] |
| $[Pt_3(CO)_6]_n^{2-}$ ($n = \sim 10, 6, 5, 4, 3, 2, 1$) | 2100–2120 (linear) 1700–1740 (bridge) | Pt carbonyl | | [49] |
| $Pt^{\delta+}$—CO | 2126 | K-L zeolite | 298 K | [50] |
| $(Pt)_7^0$ – CO | 2063 | K-L zeolite | 298 K | [50] |
| $(Pt)_5^0$ – CO | 2034 | K-L zeolite | 298 K | [50] |
| $Pt^0$—CO, $(Pt^0)_2CO$ | 2060 (linear), 2000, 1810–1840 (bridge) | K-L zeolite | 298 K | [51] |
| $Pt^{\delta+}$—CO | 2100–2120 | K-L zeolite | 298 K | [51] |
| $Pt^0$—CO | 2075–2090 (on large Pt particle) 2066, 2051, 2031 | K-L zeolite | 300 K | [52] |
| $(Pt^0)_2CO$ | 2008, 1998 | K-L zeolite | 300 K | [52] |
| $Pt^0$—CO | 1958–1976 | NaX zeolite | 300 K | [53] |
| $Pt_8$—CO | 2020 | $Pt_8$ cluster/MgO (1 1 0) | 90 K. UHV | [54] |

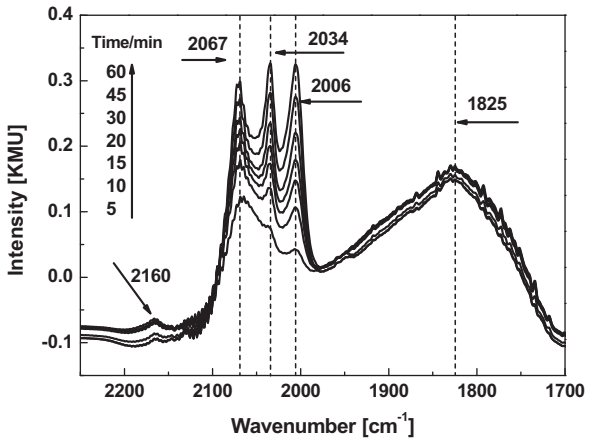


**Fig. 6.** In situ DRIFT spectra for CO adsorption recorded during in adsorption–desorption equilibrium at 300 K in a mixture of 1.5 kPa of CO in $N_2$ background.

disappeared completely. Mass spectroscopy demonstrated that the corresponding species to the unique band at 2357 $cm^{-1}$ was $CO_{2ads}$ with rising temperature to 523 K. Generally, the gas-phase $CO_2$ exhibits doublet peaks at 2361 and 2349 $cm^{-1}$, assigned to the asymmetric vibration of C=O and the same vibration with a rotation, respectively. The formation of the single peak at 2357 $cm^{-1}$ indicates that the formation of $CO_2$ occurs in the cages of zeolite *via* the following pathways (Eqs. (7)–(9)):

$$CO_{(g)} + Pt_n \rightarrow OC\text{—}Pt_n \quad (7)$$

$$1/2O_{2(g)} + Pt_n \rightarrow O\text{—}Pt_n \quad (8)$$

$$O\text{—}C\text{—}Pt_n + O\text{—}Pt_n \Longleftrightarrow Pt_n\text{—}O\cdots C\text{—}O\cdots Pt_n \rightarrow Pt_n\cdots O\text{—}C\text{—}O\cdots Pt_n \quad (9)$$

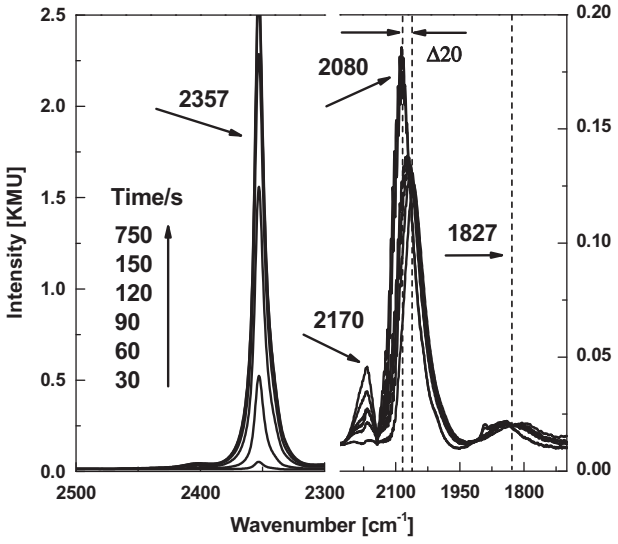


**Fig. 7.** In situ DRIFT spectra for transient co-adsorption of CO and $O_2$ (CO=$O_2$ 1.5 kPa, rest $N_2$) over the fresh reduced catalyst at 300 K.

whereas $CO_{(g)}$ and $O_{2(g)}$ represent CO and $O_2$ in the gas phase; $Pt_n$: small Pt clusters in the cages of zeolite; and OC—$Pt_n$ and O—$Pt_n$: adsorbed CO and O over the Pt surface.

Normally, CO oxidation over supported Pt catalysts unlikely occurs at room temperature because oxygen adsorption/dissociation can easily be blocked by saturated coverage of $CO_{ad}$, so called "low-rate branch." In situ DRIFTS spectra (Figs. 6 and 7) hint that the back donation of electron from the Pt clusters into the antibonding

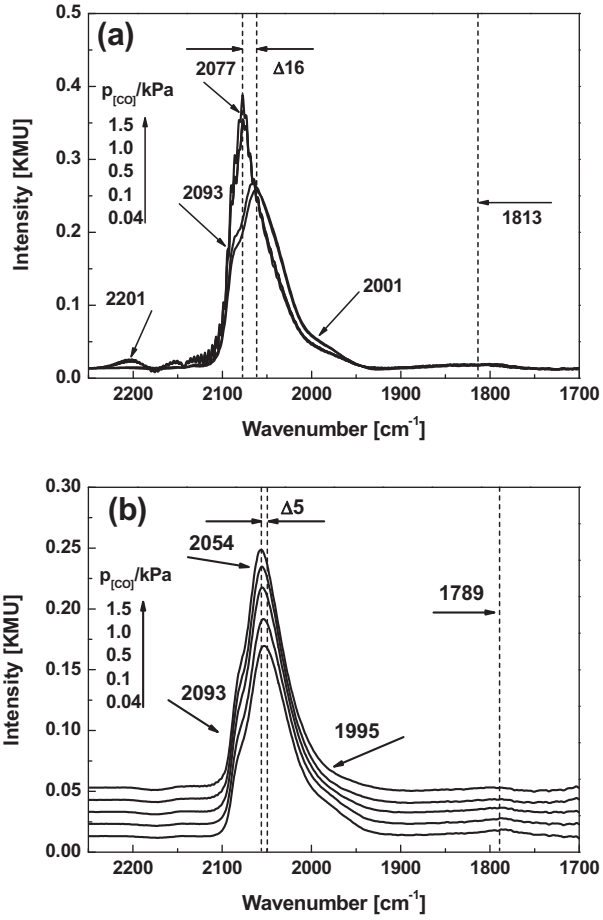


**Fig. 8.** In situ DRIFT spectra for CO adsorption at 423 K with varying CO partial pressure (mixture of $CO/N_2$) from 0.04 to 1.5 kPa (a) in a $H_2$-free atmosphere; (b) in a $H_2$-rich atmosphere, the experimental conditions are same as in the (a).

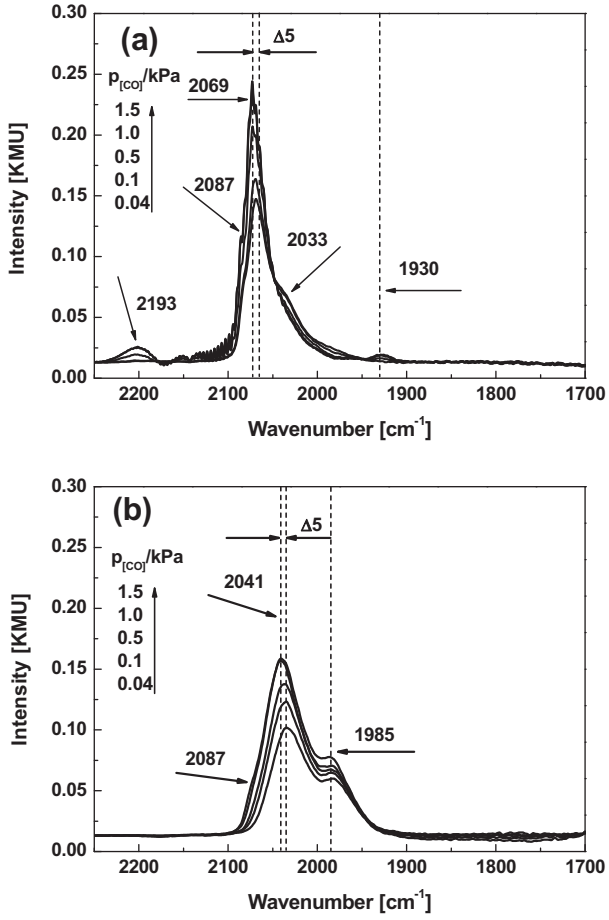


**Fig. 9.** In situ DRIFT spectra for CO adsorption at 523 K, the experimental conditions are same as in the Fig. 8. (a) in a $H_2$-free atmosphere; (b) in a $H_2$-rich atmosphere.

$\pi_g^*$ may weaken Pt—C—O bond, and the dissociation of the adsorbed $O_2$ can become easily [62]. In consequence, at room temperature, $CO_{ad}$ can be reacted with $O_{ad}$ (Eq. (3)) to form $CO_2$ molecules while its terminal oxygen atoms weakly bond to Pt clusters. $CO_2$ molecules should be constrained and only asymmetrically vibrate in the cage of zeolite. Therefore, it is understandable that only the single band at 2357 $cm^{-1}$ can be observed. However, this band did not appear in a $CO_2$ stream (1.0% $CO_2/N_2$). This fact suggests that the species may be an intermediate for CO oxidation over Pt clusters [45]. It should be emphasized here that for the first time we do observe the occurrence of CO oxidation over the Pt/NaY catalyst at room temperature. We speculate that the small Pt clusters encaged in NaY zeolite may play important role for the aimed reaction at elevated temperatures.

The similar reaction orders (Figs. 1–3), negative for CO and positive for $O_2$, were measured for both $H_2$-free and $H_2$-rich gases, but the value was slightly modified upon the temperature. These kinetic parameters are also analogy with those data reported for other Pt-based catalysts (Table 1), indicating that CO oxidation proceeds through the Langmuir–Hinshelwood mechanism in the low-rate branch. It means the Pt surfaces are fully covered with $CO_{ad}$ while $O_2$ adsorption/dissociation is strongly depressed. Furthermore, comparatively, the reaction orders varied moderately in $H_2$-rich gas. In particular, the reaction order with respect to CO became ~0 in $H_2$-rich gas at 523 K; obviously, CO adsorption was affected by the presence of $H_2$ as identified by in situ DRIFT spectra (Figs. 8–10). We assume that the adsorption of CO is suppressed by co-adsorbed $H_{ad}$ with increasing temperature, thus allows more active sites to be accessible for oxygen. If it is the case, the reaction order became less dependent on $p_{CO}$. Therefore, the CO oxidation reaction in $H_2$-rich gas can be concisely described as follows: (i) $O_2$ and CO molecules are adsorbed on the Pt surface (Eqs. (10) and (11)), (ii) $O_2$ dissociates to form $O_{ad}$, which further reacts with the neighboring $CO_{ad}$ to produce $CO_2$ (Eqs. (12) and (13), (iii) in the presence of $H_2$, $O_{ad}$ reacts with $H_{ad}$ to produce $H_2O$ as well (Eq. (14)), and (iv) $CO_2$ and $H_2O$ are desorbed from the surface (Eqs. (15) and (16)).

$$CO_{(g)} + Pt \rightarrow OC{-}Pt \quad (10)$$

$$1/2O_{2(g)} + Pt \rightarrow 1/2O_{2(g)}{-}Pt \quad (11)$$

$$1/2O_{2(g)}{-}Pt \rightarrow O_{(g)}{-}Pt \quad (12)$$

$$O{-}C{-}Pt + O{-}Pt \rightarrow CO_2{-}Pt \quad (13)$$

$$O{-}Pt + 2(H{-}Pt) \rightarrow H_2O{-}Pt \quad (14)$$

$$CO_2{-}Pt \rightarrow CO_{2(g)} + Pt \quad (15)$$

$$H_2O{-}Pt \rightarrow H_2O_{(g)} + Pt \quad (16)$$

DRIFT spectra (Fig. 10) also showed that the intensity of the linearly adsorbed CO on the Pt surface was much lower in $H_2$-rich gas than in $H_2$-free gas. $H_2$ could compete with CO on the Pt surface during reaction, this competition became strongly with increasing temperature. As a result, CO coverage decreased by ca. 20–50% (Fig. 10) in $H_2$-rich gas. In the meantime, a significant red-shift of the C—O stretch frequency from $H_2$-free (2077 $cm^{-1}$ at $P_{CO}$ = 1.5 kPa to 2061 $cm^{-1}$ at $P_{CO}$ = 0.04 kPa) to $H_2$-rich gas (2054 $cm^{-1}$ at $P_{CO}$ = 1.5 kPa to 2049 $cm^{-1}$ at $P_{CO}$ = 0.04 kPa) was also observed. The remarkable shift

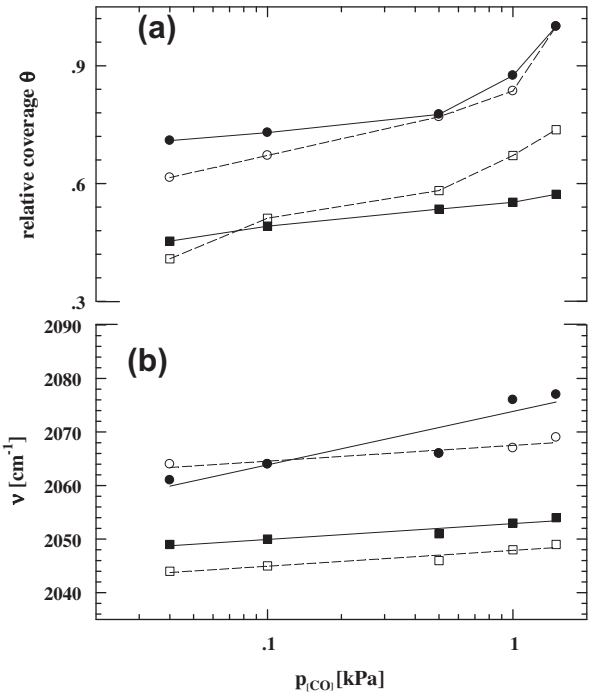


**Fig. 10.** (a) The relative CO coverage $\theta_{CO,rel}$ vs. partial pressure of CO in the $H_2$-rich and $H_2$-free gases; (b) the shift of the vibrational frequency of the linearly adsorbed CO vs. partial pressure in the $H_2$-free and $H_2$-rich atmosphere. (●) 423 K in $N_2$, (■) 423 K in $H_2$; (○) 523 K in $N_2$, (□) 523 K in $H_2$. The results are based on the spectra in Figs. 8 and 9.

may result from not only a variation of CO coverage, but also a modification of interaction between $CO_{ad}$ and $H_{ad}$ on the Pt surface.

Furthermore, several methods, such as first principles calculations [5,6], exchange of hydrogen isotope [4,63], and infrared spectroscopy [4], have been used for exploring the $H_2$ promotional effects. Some H-containing species, such as $O_2H^*$ [5,6], OH groups [4], and HCOO intermediates [64], were considered to account for the enhancement of CO oxidation. Yi et al. [63] suggested that the mechanism of CO oxidation would be different in $H_2$-rich gas over a $Au/CeO_2$ catalyst, and H-containing species produced by $H_2$ oxidation may promote CO oxidation. Using first principles calculations, Mavrikakis et al. [5,6] suggested a hydrogen-mediated ($O_2H^*$) $O_2$ activation mechanism for CO oxidation on Pt and M@Pt (M = Ru, Rh, Ir, Pd, or Au) core–shell nanocatalysts. $O_{ad}$ is proposed to be generated either by direct $O_2^* \rightarrow 2O^*$) or by H-mediated $O_2$ dissociation ($O_2^* + H^* \rightarrow O_2H^* \rightarrow O^* + OH^*$). As a result, the H-mediate $O_2$ activation is mainly responsible for the enhancement of CO oxidation. This may explain the $E_a$ = 54.0 kJ/mol in the temperature range 423–473 K in $H_2$-rich gas is lower than the $E_a$ = 82.5 kJ/mol in $H_2$-free gas. Interestingly, in $H_2$-rich gas, the $E_a$ increased to 90.0 kJ/mol when the temperature reaction increased continuously to 523 K, but the mechanism is still debatable.

## 5. Conclusions

The following conclusions can be derived for the PROX reaction over Pt/NaY zeolite catalysts:

1. In situ DRIFT spectra have demonstrated that CO oxidation over the Pt/NaY catalyst could occur at room temperature, and Pt clusters less than 1.2 nm might be responsible for this reaction. However, the role of the Pt clusters in the PROX of CO at higher temperatures is still unclear.
2. The reaction kinetics for CO oxidation in $H_2$-free gas, with negative reaction order in $p_{CO}$ ($\alpha_{CO}$ between −1.07 (423 K) and −1.22 (523 K)) and positive order in $p_{O_2}$ ($\alpha_{O_2}$ between 0.65 (423 K) and 0.78 (523 K)), are consistent with the Langmuir–Hinshelwood mechanism in the oxygen-limited low-rate branch.
3. In $H_2$-rich gas, the reaction order with respect to CO increases from −0.48 to ∼0 with increasing temperature (423–523 K) and the $O_2$ reaction order decreases slightly, from 0.74 to 0.56, an indicative of a gradual transition from the oxygen-limited low-rate branch to the CO-limited high-rate branch. A change in mechanism with higher temperature is also indicated by the nonlinear behavior of the logarithmic reaction rates $r_{CO}$ vs. $1/T$, which can approximately be described by $E_a$ of 54.0 ± 4.0 kJ/mol at temperatures up to 473 K and of 90.0 ± 5.0 kJ/mol above that temperature.
4. Based on in situ DRIFTS measurements, CO interaction with the Pt/NaY zeolite catalyst is dominated by linearly adsorbed CO species adsorbed on metallic $Pt^0$ nanoparticles. A significant red-shift of CO stretch frequency was observed in the presence of $H_2$, which revealed that the interaction between Pt—CO bond and adsorption hydrogen occurred, possibly being responsible for the enhancement of CO oxidation.

## Acknowledgments

The authors are grateful to the support from the Chinese Education Ministry 111 Project (B08021), the National Natural Science Foundation of China (21176071, 21106041), Shanghai PuJiang Talent Program (2010/10PJ1402500, 2011/11PJ1402400), Program of Science and Technology Commission of Shanghai Municipality (11JC1402700) Innovation Program of Shanghai Municipal Education Commission (11ZZ52, 11ZZ051), Shanghai Natural Science Foundation (11ZR1408400), Opening Project Program of State Key Laboratory of Chemical Engineering (SKL-ChE-10C05), and Fundamental Research Funds for the Central Universities.

## Appendix A. Supplementary material

Supplementary data associated with this article can be found, in the online version, at doi:10.1016/j.jcat.2011.12.012.

## References

[1] S. Kawatsu, J. Power Sources 71 (1998) 150.
[2] S.H. Oh, R.M. Sinkevitch, J. Catal. 142 (1993) 254.
[3] D.L. Trimm, Z.I. Önsan, Catal. Rev. 43 (2001) 31.
[4] A. Fukuoka, J. Kimura, T. Oshio, Y. Sakamoto, M. Ichikawa, J. Am. Chem. Soc. 129 (2007) 10120.
[5] S. Alayoglu, A.U. Nilekar, M. Mavrikakis, B. Eichhorn, Nat. Mater. 7 (2008) 333.
[6] A.U. Nilekar, S. Alayoglu, B. Eichhorn, M. Mavrikakis, J. Am. Chem. Soc. 132 (2010) 7418.
[7] Y.-F. Han, M. Kahlich, M. Kinne, R.J. Behm, Appl. Catal. B 52 (2004) 123.
[8] Y.-F. Han, M. Kahlich, M. Kinne, R.J. Behm, Appl. Catal. B 50 (2004) 209.
[9] J. Xu, T. White, P. Li, C. He, J. Yu, W. Yuan, Y.-F. Han, J. Am. Chem. Soc. 13 (2010) 10398.
[10] J. Xu, P. Li, X. Song, Z. Qi, J. Yu, W. Yuan, Y.-F. Han, Ind. Eng. Chem. Res. 49 (2010) 4149.
[11] K. Ramesh, L. Chen, F. Chen, Y. Liu, Z. Wang, Y.-F. Han, Catal. Today 131 (2008) 477.
[12] Y.-F. Han, Z. Zhong, K. Ramesh, F. Chen, L. Chen, J. Phys. Chem. C 111 (2007) 3163.
[13] Y.-F. Han, M.J. Kahlich, M. Kinne, R.J. Behm, Phys. Chem. Chem. Phys. 4 (2002) 389.
[14] M.J. Kahlich, H.A. Gasteiger, R.J. Behm, J. Catal. 171 (1997) 93.
[15] M.M. Schubert, M.J. Kahlich, H.A. Gasteiger, R.J. Behm, J. Power Sources 84 (1999) 175.
[16] D.H. Kim, M.S. Lim, Appl. Catal. A 224 (2002) 27.
[17] B. Qiao, A. Wang, X. Yang, L.F. Allard, Z. Jiang, Y. Cui, J. Liu, J. Li, T. Zhang, Nat. Chem. 3 (2011) 634.

[18] O. Pozdnyakova, D. Teschner, A. Wootsch, J. Kröhnert, B. Steinhauer, H. Sauer, L. Toth, F.C. Jentoft, A. Knop-Gericke, Z. Paál, R. Schlögl, J. Catal. 237 (2006) 1.
[19] M. Watanabe, H. Uchida, H. Igarashi, M. Suzuki, Chem. Lett. (1995) 21.
[20] H. Igarashi, H. Uchida, M. Suzuki, Y. Sasaki, M. Watanabe, Appl. Catal. A 159 (1997) 159.
[21] H. Igarashi, H. Uchida, M. Watanabe, Chem. Lett. (2000) 1262.
[22] M. Watanabe, H. Uchida, K. Ohkubo, H. Igarashi, Appl. Catal. B 46 (2003) 595.
[23] M. Kotobuki, A. Watanabe, H. Uchida, H. Yamashita, M. Watanabe, Appl. Catal. A 307 (2006) 275.
[24] N. Maeda, T. Matsushima, H. Uchida, H. Yamashita, M. Watanabe, Appl. Catal. A 341 (2008) 93.
[25] S. Huang, K. Hara, Y. Okubo, M. Yanagi, H. Nambu, A. Fukuoka, Appl. Catal. A 365 (2009) 268.
[26] H. Kacirek, H. Lechert, J. Phys. Chem. 79 (1975) 1589.
[27] N.I. Jaeger, A.L. Jourdan, G. Schulz-Ekloff, J. Chem. Soc. Faraday Trans. 87 (1991) 1251.
[28] P.B. Weisz, Chem. Eng. Prog. Symp. Ser. 55 (1992) 29.
[29] H. Muraki, S.-I. Matunaga, H. Shinjoh, M.S. Wainwright, D.L. Trimm, J. Chem. Technol. Biotechnol. 52 (1991) 415.
[30] J. Sarkany, R.D. Gonzalez, Appl. Catal. 5 (1983) 85.
[31] N.W. Cant, P.C. Hicks, B.S. Lennon, J. Catal. 54 (1978) 372.
[32] Z. Paal, P. Tetenyi, Appl. Surf. Sci. 14 (1982–1983) 307.
[33] M. Peuckert, H.P. Bonzel, Surf. Sci. 145 (1984) 239.
[34] J.F. Moulder, W.F. Stickle, P.E. Sobol, K.D. Bomben, in: J. Chastain, C. King Jr (Eds.), Handbook of X-ray Photoelectron Spectroscopy, Physical Electronics, Inc., 1995. ISBN:0-9648124-1-X.
[35] S.H. Park, M.S. Tzou, W.M.H. Sachtler, Appl. Catal. 24 (1986) 85.
[36] C. Klünker, M. Balden, S. Lehwald, W. Daum, Surf. Sci. 360 (1996) 104.
[37] J. Yoshinobu, M. Kawai, Surf. Sci. 363 (1996) 105.
[38] R.G. Greenler, K.D. Burch, K. Kretzschmar, R. Klauser, A.M. Bradshaw, B.E. Hayden, Surf. Sci. 152/153 (1985) 338.
[39] D.M. Haaland, Surf. Sci. 185 (1987) 1.
[40] R. Barth, R. Pitchai, R.L. Anderson, X.E. Verykios, J. Catal. 116 (1989) 61.
[41] M. Primet, J. Catal. 88 (1984) 273.
[42] G.-J. Li, T. Fujimoto, A. Fukuoka, M. Ichikawa, J. Chem. Soc., Chem. Commun. (1991) 1337.
[43] F.-W. Schütze, F. Rößner, Z. Phys. Chem. 191 (1995) 271.
[44] H. Bischoff, N.I. Jaeger, G. Schulz-Ekloff, L. Kubelkova, J. Mol. Catal. 80 (1993) 95.
[45] D.A. Mantell, K. Kunimori, S.B. Ryali, G.L. Haller, J.B. Fenn, Surf. Sci. 172 (1986) 281.
[46] V.B. Kazansky, V.Yu. Borovkov, N. Sokolova, N.I. Jaeger, G. Schulze-Ekloff, Catal. Lett. 23 (1994) 263.
[47] K. Klier, Langmuir 4 (1988) 13.
[48] J.S. Bradley, J.M. Millar, E.W. Hill, S. Behal, J. Catal. 129 (1991) 530.
[49] G. Longoni, P. Chini, J. Am. Chem. Soc. 98 (1976) 7225.
[50] M.J. Kappers, J.H. van der Maas, Catal. Lett. 10 (1991) 365.
[51] C. Besoukhanova, J. Guidot, D. Barthomeuf, M. Breysse, J.R. Bernard, J. Chem. Soc., Faraday Trans. I 77 (1981) 1595.
[52] L.M. Kustov, D. Ostgard, W.M.H. Sachtler, Catal. Lett. 9 (1991) 121.
[53] A.I. Serykh, O.P. Tkachenko, V.Y. Borovkov, V.B. Kazansky, M. Beneke, N.I. Jaeger, G. Schulz-Ekloff, Phys. Chem. Chem. Phys. 2 (2000) 5647.
[54] U. Heiz, A. Sanchez, S. Abbet, W.-D. Schneider, Chem. Phys. 262 (2000) 189.
[55] U. Heiz, A. Sanchez, S. Abbet, W.-D. Schneider, J. Am. Chem. Soc. 121 (1999) 3214.
[56] Y. Shi, K.M. Ervin, J. Chem. Phys. 108 (1998) 1757.
[57] H.-J. Freund, G. Meijer, M. Scheffler, R. Schlögl, M. Wolf, Angew. Chem. Int. Ed. 50 (2011) 10064.
[58] B.C. Gates, Chem. Rev. 95 (1995) 511.
[59] J. de Graat, A.J. van Dillen, K.P. de Jong, D.C. koningsberger, J. Catal. 203 (2001) 307.
[60] A.L. Ankudinov, J.J. Rehr, J.J. Low, S.R. Bare, J. Chem. Phys. 116 (2002) 1911.
[61] M.J. Lundwall, S.M. McClure, D.W. Goodman, J. Phys. Chem. C 114 (2010) 7904.
[62] J. Wintterlin, S. Völkening, T.V.W. Janssens, T. Zambelli, G. Ertl, Science 278 (1997) 1931.
[63] G. Yi, H. Yang, B. Li, H. Lin, K. Tanaka, Y. Yuan, Catal. Today 157 (2010) 83.
[64] K. Tanaka, M. Shou, H. He, X. Shi, X. Zhang, J. Phys. Chem. C 113 (2009) 12427.